

bradscholars

An experimental and simulation comparison of a 3-D abrupt contraction flow using the Molecular Stress Function constitutive model

Item Type	Article
Authors	Olley, Peter;Gough, Tim;Spares, R.;Coates, Philip
Citation	Olley P, Gough TD, Spares R et al (2021) An experimental and simulation comparison of a 3-D abrupt contraction flow using the Molecular Stress Function constitutive model. <i>Plastics, Rubber and Composites</i> . 50(1): 18-34.
DOI	https://doi.org/10.1080/14658011.2020.1826195
Publisher	Maney Publishing
Rights	© 2021 Taylor & Francis. The Version of Record of this manuscript has been published and is available in <i>Plastics, Rubber and Composites</i> , date of publication (https://doi.org/10.1080/14658011.2020.1826195)
Download date	2026-05-12 19:06:16
Link to Item	https://bradscholars.brad.ac.uk/handle/10454/18042.2

An experimental and simulation comparison of a 3-D abrupt contraction flow using the Molecular Stress Function constitutive model

P. Olley¹, T. Gough, R. Spares², P.D. Coates

Faculty of Engineering & Informatics, University of Bradford, UK

abstract

The Molecular Stress Function (MSF) constitutive model with convective constraint release mechanism has been shown to accurately fit a large range of viscometric data, and also shown to give strong vortex growth in flows of LDPE through planar and axisymmetric contractions. This work compares simulation and experimental results for 3-D flows of Lupolen 1840H LDPE through a contraction slit; 3-D effects are introduced by using a slit with a low upstream aspect ratio of 5:3.

Comparisons are made with vortex opening angles obtained from streak photography, and also with stress birefringence measurements. The comparisons are made with two versions of the convective constraint release (CCR) mechanism. The simulated vortex angles for one version of the CCR mechanism are found to approach what is seen experimentally. The best-fit value for the stress optical coefficient was found to vary between CCRs and to decrease with flow rate. This is partially explained by different centreline elongational rates with the two CCRs, which in turn is related to different opening angles.

A 3-D simulation is compared to the corresponding 2-D simulation. It is shown that both velocity vectors and birefringence show only small changes to around 60% of the distance to the side wall.

Keywords: Simulation, birefringence, streak photography, opening angle, molecular stress function, convective constraint release, stress optical coefficient, vortex growth.

1. Introduction and background

Simulation of viscoelastic flows of polymer melts have advanced considerably with the introduction of molecularly based constitutive models. A molecularly based model, the Molecular Stress Function (MSF) model [1 - 3] uses an energy balance approach and has been shown to accurately fit rheometric data for branched and un-branched polymers in uniaxial, planar and biaxial elongation. Some over-prediction of first normal stress difference was seen for these models, however a particular model [4] uses a form of the convective constraint release (CCR) mechanism of Marrucci [5] and has been shown to accurately fit all rheometric measurements for a number of branched and un-branched polymers using only two adjustable parameters. We refer to this model as the MSF-CCR model. In particular the model has been shown to fit a wide range of rheometric data for the well-characterized IUPAC Melt A LDPE and to give strong vortex growth in axisymmetric and planar abrupt contraction flows [6].

Molecular considerations have figured strongly in other rheological modelling such as the time-integral Pom-Pom model [7, 8], and also in differential models [9, 10]. Stress induced birefringence has been employed to assess accuracy of computed stresses for (predominantly) planar flows [11 - 15] and for 3-D flows [16 - 19]. Birefringence arises when a materials refractive indices are anisotropic, which is believed to occur in polymers due to the molecular orientation and molecular stretch [16, 20]. These two properties are directly linked to polymer stress in the constitutive models mentioned

¹ email: p.olley@bradford.ac.uk

² Now at Covvi, Leeds, UK

above, and the stress-optical law makes a quantitative link between the stress tensor and the refractive index tensor. The stress-optical law can thus be considered as semi-empirical [16]. Detailed studies performing birefringence with simultaneous force-based stress measurements have generally confirmed the validity of the stress optical law for polymer melts, but have also noted non-linearities (and thus variation of the stress optical coefficient) in some circumstances including a reduction in the stress optical coefficient for strains greater than around 2 [21], and also a variation of the stress optical coefficient with strain-rate once the non-linear strain region is reached [22].

We examine the accuracy of the MSF-CCR model in comparison with experimental results for an abrupt contraction die with significant 3-D effects. The performance of the model has been established in ref [6] for 2-D and axisymmetric flows for IUPAC Melt A LDPE, but the authors are not aware of comparable assessment in 3-D flows. The original IUPAC Melt A polymer is now widely considered to be affected by age, hence a polymer considered to be its “analogue” - Lupolen 1840H - is studied.

2. Experimental

Full details of the experimental birefringence method have been given in Ref. [15]. For context an outline description of the birefringence method is included here, along with a description of other experimental methods used by the current work.

Flow birefringence experiments were performed using a commercial polymer single screw extruder (Betol BC38) with a 4:1 contraction ratio slit. The slit is ‘planar’ in cross-section but with significant 3-D effects induced by the 5:3 width to height ratio (as measured upstream of the contraction). Borosilicate glass was used for the walls of the flow cell; the same glass was also used in a slit in the top surface to allow illumination from above. A rectangular channel of 100mm length separated the outlet of the extruder from the inlet of the flow cell. The dimensions of the flow cell are shown in Figure 1.

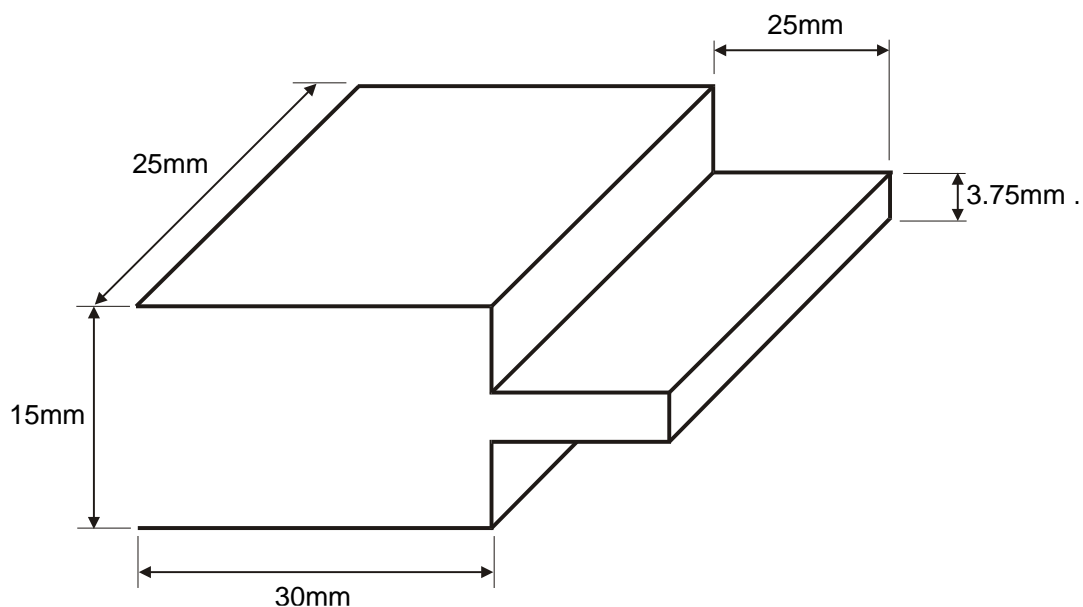


Figure 1 Dimensions of 4:1 contraction in flow visualisation cell (not to scale).

The flow cell was arranged with polarisers and $\lambda/4$ plates as shown in Figure 2. A mercury vapour lamp was used as a light source, and a 546 nm narrowband interference filter was placed in front of the camera lens to remove other wavelengths from the spectrum.

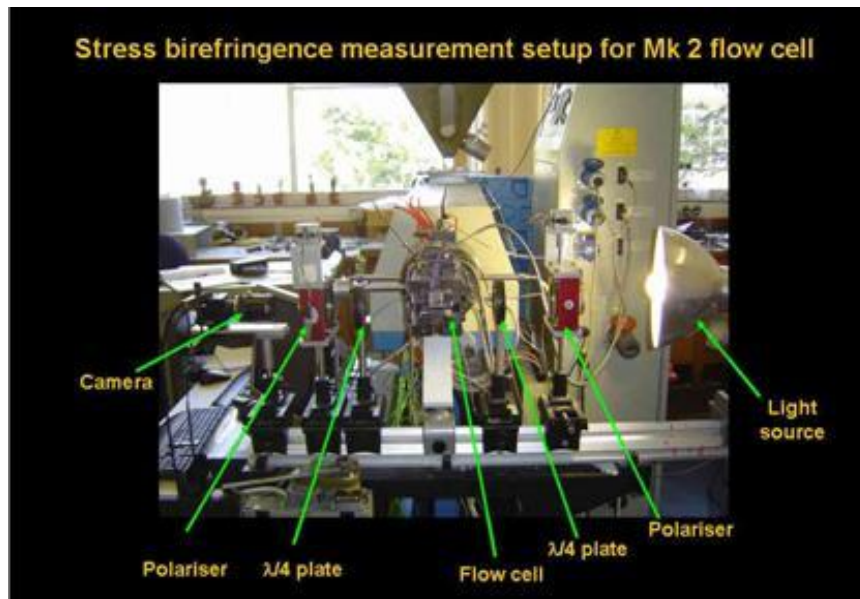


Figure 2 Arrangement of flow cell for birefringence measurements.

In addition to birefringence measurements, streak photography was used to identify vortex sizes and opening angles. Ballontini glass tracer particles with a typical size of $50\mu\text{m}$ were introduced into the flow at low concentration levels (0.5% by weight). The centreline of the flow was illuminated using a 30mW HeNe laser with an Edmund Optic line generator lens mounted in line with the illuminating top window. This produced a laser sheet in the centre plane of the die with a width of approximately 1mm. A 25 frames per second CCD camera was used to record the process continuously. This method allows those particles in the centre of the die to be identified photographically. It was possible to modulate the concentration of glass particles by adding batches of polymer with, and without, glass tracer particles to the hopper of the extruder. It was noted that the vortex tended to keep the concentration of glass particles it had when the vortex was first formed, hence this modulation method was used to obtain a more clear contrast between the vortex and the main flow. Recording with a finite aperture time showed the particles as a streak, whose length indicates their speed. It was possible to positively identify the line between the faster particles in the main flow, and the slower particles in the vortex, which permitted the vortex boundary to be identified and the vortex opening angle to be measured.

The polymer used was Lupolen 1840H LDPE. Experiments were performed at 150°C at a number of extruder flow rates. The minimum rate of the extruder screw that gave a steady flow was 5 revolutions per minute (rpm) – below this speed there was a tendency for the flow to pulsate slightly. The maximum usable rate was set by the strength of the glass and the seals of the flow cell, and was found to be 40 rpm. At each rotation rate the mass flow rate was determined by directly measuring the mass of polymer output over approximately one minute. Steady state birefringence images were captured for each flow rate. Following this a batch of the same polymer mixed with the glass tracer particles was introduced into the extruder and, using the modulation method described above, a series of photographs was taken at the corresponding flow rates.

To characterise key behaviour of the particular batch of Lupolen 1840H that was used, the storage and loss moduli (G' and G'') were measured. The measurements were made using 25 mm parallel plate geometry mounted on an Anton Paar MCR501 rheometer at 150°C . Two frequency sweeps were

performed between values of 0.0158 rads/s and 100 rads/s within the linear viscoelastic regime (as proven through amplitude sweeps). The resulting data was fitted using the Maxwell model:

$$G'(\omega) = \sum_{i=1}^N g_i \frac{\omega^2 \lambda_i^2}{1 + \omega^2 \lambda_i^2}, \quad (1)$$

and
$$G''(\omega) = \sum_{i=1}^N g_i \frac{\omega \lambda_i}{1 + \omega^2 \lambda_i^2}. \quad (2)$$

using the method of ref. [23]. A range of λ values was used to cover the range informed by the G' , G'' data. A spectrum of 8 relaxation times between relaxation times of 10^{-3} s and 10^2 s was produced, as given in Table 1.

i	λ_i (s)	g_i (Pa)
1	1.000×10^{-3}	1.280×10^5
2	5.179×10^{-3}	5.792×10^4
3	2.683×10^{-2}	3.303×10^4
4	1.389×10^{-1}	1.844×10^4
5	7.197×10^{-1}	8.772×10^3
6	3.728×10^0	3.564×10^3
7	1.931×10^1	9.874×10^2
8	1.000×10^2	1.677×10^2

Table 1 Relaxation spectrum obtained from G' and G'' data of Lupolen 1840H at 150°C

The values of G' and G'' returned by equations (1) and (2), using the above relaxation spectrum, are shown in Figure 3, and show an excellent fit to the original experimental data.

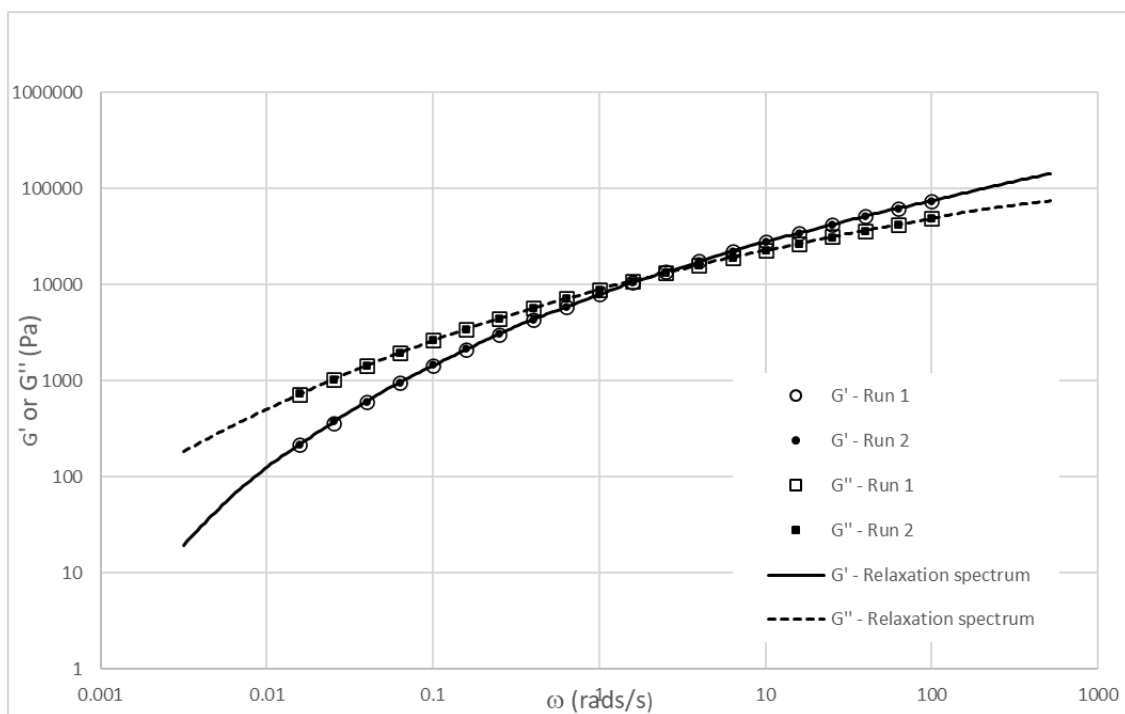


Figure 3 G' and G'' data from two experimental runs, and the predictions from the derived relaxation spectrum.

The spectrum gives a low-rate shear viscosity of $\eta_0 = 5.93 \times 10^4$ Pa.s. This is consistent with the value of $5.9 \pm 0.3 \times 10^4$ Pa.s given by [24]. The same reference points out this value is significantly higher than the low-rate shear viscosity of IUPAC Melt A (5.2×10^4 Pa.s).

Sentmanat et al [24] give uniaxial extensional data for Lupolen 1840H, and also give independent data for G' and G'' . Their G' and G'' data is plotted in Figure 4 against the values from the relaxation spectrum in Table 1. An excellent level of agreement is seen in the cross-comparison giving confidence that the batch of Lupolen 1840H used in the current experiments is very similar to that used for their extensional measurements.

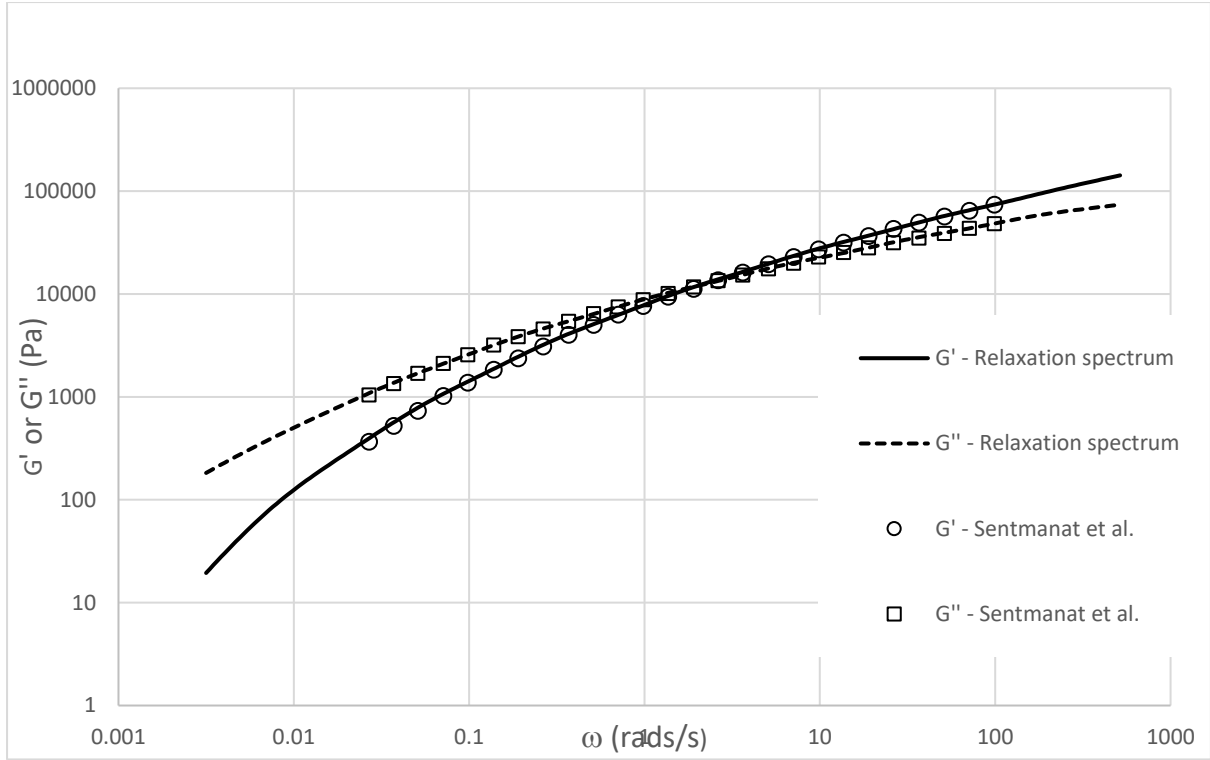


Figure 4 Cross-comparison of G' and G'' data of Sentmanat et al. [24] and relaxation spectrum obtained using new G' and G'' data

3. Constitutive model and parameter estimation

The constitutive model used in this work is the Molecular Stress Function model with Convective Constraint Release (MSF-CCR) [25]. The model takes the form

$$\boldsymbol{\tau}(t) = \int_{-\infty}^t m(t, t') \mathbf{S}_{\text{MSF}}(t, t') dt', \quad (3)$$

where $m(t, t')$ is the memory function between time t' in the past and the current time t (commonly represented by a spectrum of relaxation times and relaxation moduli), and

$$\mathbf{S}_{\text{MSF}}(t, t') = f^2(t, t') \mathbf{S}_{\text{DE}}(t, t'), \quad (4)$$

where $\mathbf{S}_{\text{DE}}(t, t')$ is the Doi-Edwards strain tensor and $f(t, t')$ represents a ratio of tube diameters a_0/a , where a is the tube diameter at the current time t , and a_0 is the tube diameter when the tube was created at time t' in the past. To calculate the contribution from a particular past time t' , one starts from t' with a value of $f = 1$, and calculates forwards in time to the current time t according to

$$\frac{\partial f^2}{\partial t} = \frac{\beta f^2}{1 + \frac{\beta-1}{f^4}} \left(\mathbf{k} : \mathbf{S} - \frac{1}{f^2-1} CR \right). \quad (5)$$

In equation (5) \mathbf{k} is the velocity gradient tensor (given by $k_{ij} = \partial u_i / \partial x_j$), \mathbf{S} is the orientation tensor, β is a parameter that is equal to 1 for linear melts, and normally equal to 2 to strain hardening melts

($\beta=2$ is used here), and the term CR is a form of convective constraint release. The constraint release mechanism is expressed in term of the Rivlin-Ericksen tensors, \mathbf{A}_1 and \mathbf{A}_2 .

$$CR = \frac{1}{2}(f^2 - 1)^2 \left[a_1 \frac{1}{2} \sqrt{\mathbf{A}_1^2 : \mathbf{S}} + a_2 \frac{1}{2} \sqrt{|\mathbf{A}_2 : \mathbf{S} - \mathbf{A}_1^2 : \mathbf{S}|} \right], \quad (6)$$

where a_1 and a_2 are parameters that control constraint release, predominantly in irrotational and rotational flows respectively [4]. The Rivlin-Ericksen tensors are given by

$$\mathbf{A}_1^2 = 4\mathbf{D}^2, \quad (7)$$

$$\text{and } \mathbf{A}_2 = \frac{D\mathbf{A}_1}{Dt} + \mathbf{A}_1^2 + 2(\mathbf{W} \cdot \mathbf{D} + \mathbf{D} \cdot \mathbf{W}^T), \quad (8)$$

where \mathbf{W} and \mathbf{D} are the rate of rotation tensor, and the rate of deformation tensor respectively, given by $\mathbf{W} = (\mathbf{k} - \mathbf{k}^T)/2$ and $\mathbf{D} = (\mathbf{k} + \mathbf{k}^T)/2$.

A variation of the constraint release mechanism was given in Ref [6] as

$$CR = \frac{1}{2}(f^2 - 1)^2 \left[a_1 \frac{1}{2} \sqrt{\mathbf{A}_1^2 : \mathbf{S}} + \frac{a_2}{f^4} \frac{1}{2} \sqrt{|\mathbf{A}_2 : \mathbf{S} - \mathbf{A}_1^2 : \mathbf{S}|} \right]. \quad (9)$$

The modification to the constraint release mechanism gives no change in constant rate elongational flow, since the term $\mathbf{A}_2 : \mathbf{S} - \mathbf{A}_1^2 : \mathbf{S}$ is then zero, but it reduces dissipation of extensional effects in mixed shear and elongational flow, such as may occur in a contraction. In this work we refer to the constraint release mechanism given in equation (6) as 'CR1', and the constraint release mechanism given in equation (9) as 'CR2'.

For the "analogue" of Lupolen 1840H, IUPAC Melt A, the parameters $a_1 = 0.012$ and $a_2 = 0.07$ (for CR1), and $a_1 = 0.012$ and $a_2 = 0.55$ (for CR2) were shown to give a good fit to several rheometric data sets [6]. To obtain a fit for Lupolen 1840H we first consider the elongational data of Sentmanat et al [24] who made uniaxial elongational measurements of Lupolen 1840H at 150°C. These data are shown in Figure 5; it was reported that necking was clearly observed during the tests which caused the transient viscosity to drop beyond certain points. Only data points before the onset of these drops in apparent viscosity are shown in Figure 5. The figure also shows the predictions of the MSF-CCR model using the relaxation spectrum of Table 1 and the parameter $a_1 = 0.012$ as used for IUPAC Melt A (the parameter a_2 is not relevant for these plots because the term it multiplies in both equations (6) and (9) is zero in constant strain rate elongational flows [4]). Hence the MSF-CCR predictions are identical using either CR1 or CR2 in this flow. The parameter a_1 has a major effect on the level of the final "steady-state" plateau viscosities, but little effect on the gradients up to reaching those plateaus. Sentmanat et al. state that the polymer was observed to "neck" before any steady-state viscosity was achieved, hence we retain the (analogue) IUPAC Melt A value of $a_1 = 0.012$ for this work.

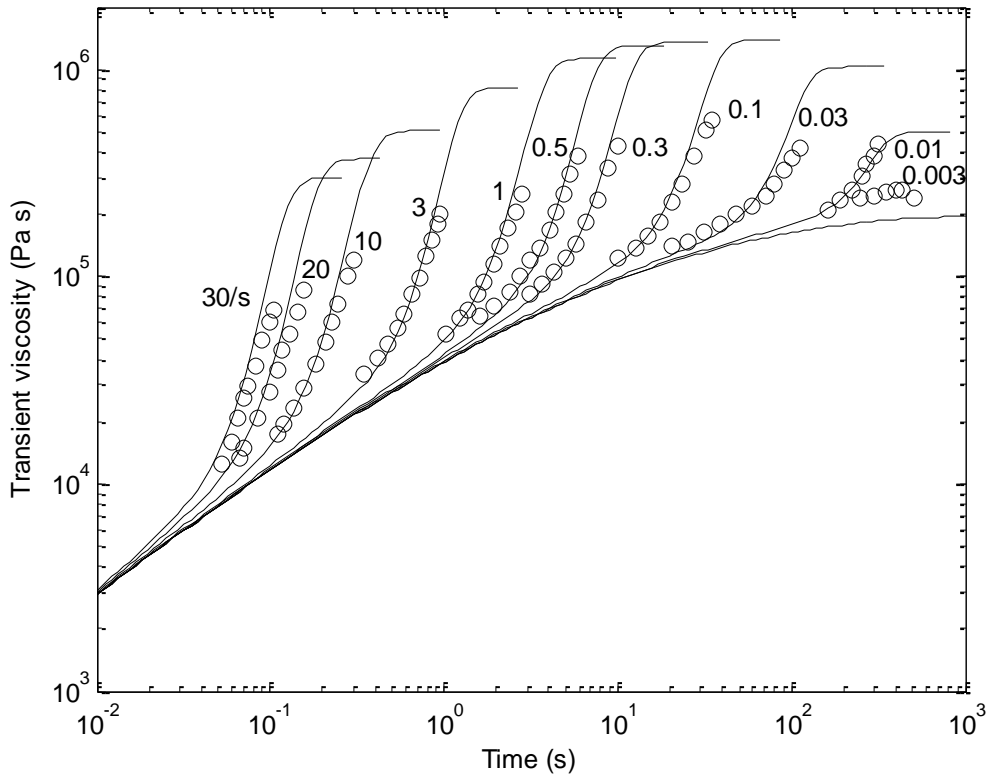


Figure 5 Comparison of Uniaxial Elongational measurements of Lupolen 1840H at 150°C (from [24]) at a range of elongational rate and the predictions of the MSF-CCR model with IUPAC Melt A appropriate parameters

The uniaxial data of Sentmanat et al had been benchmarked against data from [25] demonstrating very good agreement up to elongational rates of 10/s. With one exception the predictions of the MSF-CCR using IUPAC Melt A appropriate parameters are also in very good agreement to around 10/s, with some deviation above this rate; the exception is at a rate of 0.003/s for which experimental results clearly show more strain hardening. The difference at this rate is not surprising because the longest time constant in the relaxation spectrum is 1×10^2 s, and so the ability to give a strain hardening response falls away for rates below approximately 10^{-2} s^{-1} (the inverse of the longest time constant).

Shear viscosity data is needed to establish values for the parameter α_2 in CR1 and CR2. Zatloukal gives shear viscosity data for Lupolen 1840H at 180°C in Ref. [26]. As the data is measured at 180°C it needs time-temperature shifting to 150°C for a comparison to be made. The required shift factor, a_T , can be directly determined from

$$a_T = \frac{\eta_T}{\eta_0}, \quad (10)$$

where η_0 is the low-rate shear viscosity at the original measurement temperature, and η_T is the low rate shear viscosity at the temperature the results are to be mapped to. From the relaxation spectrum given in [26] the low-rate shear viscosity at 180°C was 1.95×10^4 Pa s. At 150°C we obtained 5.93×10^4 Pa s, hence equation (10) gives the shift factor to be 3.04 between the two temperatures.

Figure 6 shows the shear data from [26] and the same data after time-temperature shifting to 150°C, and compares the latter against the predictions of the MSF-CCR model at 150°C using the relaxation

spectrum of Table 1. A value of $a_1 = 0.012$ was used as before, and the best ‘by-eye’ fits were found for a_2 which were $a_2 = 0.11$ with constraint release mechanism CR1, and $a_2=0.65$ for CR2. The curves for CR1 and CR2 are almost identical (to graphical scale) with these parameters.

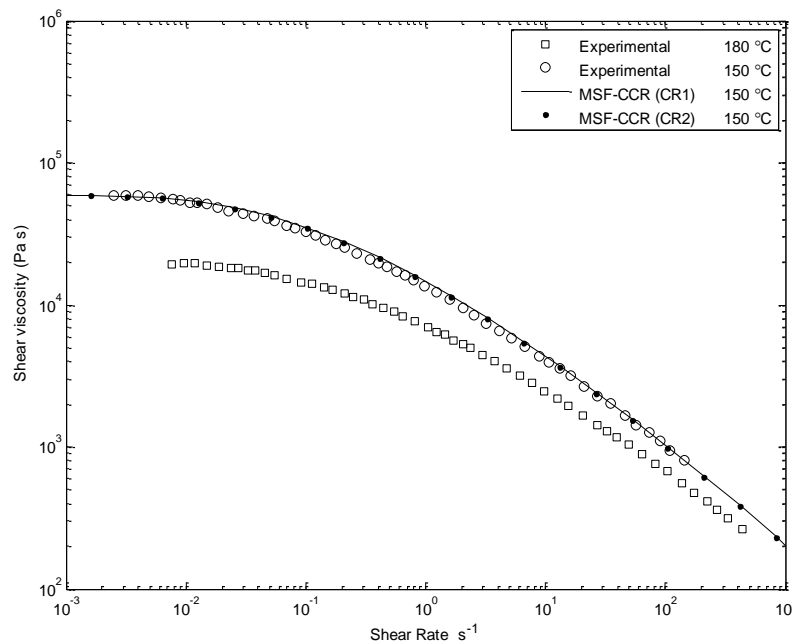


Figure 6 Shear viscosity measurements of Lupolen1840H [26] and the same data after time-temperature shifting to 150°C, compared with predictions of the MSF-CCR model at 150°C using CCR mechanisms CR1 and CR2

It is worth noting that the corresponding IUPAC Melt A parameters for a_2 gave a reasonable (though fractionally high) fit to this Lupolen 1840H data. The IUPAC Melt A parameters were $a_2 = 0.07$ for CR1 and 0.55 for CR2.

4. 3-D Modelling

Details of our simulation for the MSF-CCR constitutive equation in 2-D or axisymmetric flows are given in Ref. [6]. An outline of this simulation method is given here, along with detailed descriptions about the particular differences for simulating a 3-D flow.

Mesh and tracking

For 2-D modelling it is very common to use 9-noded bi-quadratic elements for velocity components, with pressure implemented one order of interpolation lower, using 4-noded bi-linear elements. For 3-D we use the natural extrapolation of this approach using 27-noded tri-quadratic elements for velocity components and 8-noded tri-linear elements for pressure.

In order to calculate the current stress, $\boldsymbol{\tau}(t)$ at a given point, according to equation (3), it is necessary to track the position of the particle of polymer back in time, from the current time, t , to times in the past, t' . The Doi-Edwards strain tensor of equation (4) can be calculated from the deformation gradient tensor, $\mathbf{F}(t, t')$, which can be calculated along this path using:

$$\frac{d\mathbf{F}(t,t')}{dt'} = \mathbf{k}(t')\mathbf{F}(t,t'), \quad (11)$$

where $\mathbf{k}(t')$ is the velocity gradient tensor evaluated at time t' .

To compute the particle's trajectory backwards in time the particle's position at a time $\delta t'$ earlier is calculated according to the standard kinematic procedure:

$$\begin{aligned} x(t' - \delta t') &= x(t') - u \delta t' + \frac{\delta t'^2}{2} \left(u \frac{\partial u}{\partial x} + v \frac{\partial u}{\partial y} + w \frac{\partial u}{\partial z} \right), \\ y(t' - \delta t') &= y(t') - v \delta t' + \frac{\delta t'^2}{2} \left(u \frac{\partial v}{\partial x} + v \frac{\partial v}{\partial y} + w \frac{\partial v}{\partial z} \right), \\ z(t' - \delta t') &= z(t') - w \delta t' + \frac{\delta t'^2}{2} \left(u \frac{\partial w}{\partial x} + v \frac{\partial w}{\partial y} + w \frac{\partial w}{\partial z} \right), \end{aligned} \quad (12)$$

where u , v and w are the velocity components in the x , y and z directions respectively. For accuracy the time step, $\delta t'$, was limited so that a distance step was never greater than $1/10^{\text{th}}$ of local element dimension. In 2-D flows it is possible to use the 2-D streamfunction to correct minor inaccuracies in tracking [27], however there is no comparable streamfunction available for 3-D flows. In Appendix 1 we assess the effect on results of using only kinematic tracking, by comparing results for a 2-D flow both with and without the streamfunction correction. It is shown that over a large range of flow rates there is a maximum difference in opening angle of approximately 0.5° from using the two tracking methods, and negligible differences to contour plots of principal stress difference, hence it is reasonable to expect only very slight effects on the (closely related) computed birefringence images.

Computation of \mathbf{S}_{MSF} and velocity and pressure fields

Calculating the deformation gradient tensor along a particle's history (using equations (12) and (11)) allows the Doi-Edwards strain tensor, $\mathbf{S}_{DE}(t, t')$ to be calculated using Currie's approximation [28]. The computation of $f^2(t, t')$ for equation (4) is rather different since having tracked backwards in time to a time t' in the past, f^2 must then be calculated *forwards* in time, starting with the value $f^2 = 1$ at time t' and then integrated forwards to the current time t according to equation (5) to obtain $f^2(t, t')$ - see Ref. [6] for details. Knowing both $\mathbf{S}_{DE}(t, t')$ and $f^2(t, t')$ allows $\mathbf{S}_{MSF}(t, t')$ to be calculated according to equation (4); repeating this for all times t' in the particle's strain history (up to certain limits, see Ref. [6]) allows the stress to be calculated according to equation (3).

Performing this stress computation at all required points (at the Gauss points of each element in this implementation) allows the velocity and pressure fields to be updated. For this we use an iterative finite element procedure. For an assumed steady-state solution we require a velocity field that produces a viscoelastic stress field, $\boldsymbol{\tau}$ ($\boldsymbol{\tau}$ is the stress field calculated using equation (3)), where

$$\nabla \cdot (\boldsymbol{\tau} - \mathbf{I} p) = 0, \quad (13)$$

where p is pressure and \mathbf{I} is the identity matrix. Following the method of Ref. [29] we subtract notional Newtonian stresses of comparable magnitude from each side of equation (13), giving:

$$-\nabla \cdot (\mu(\mathbf{L} + \mathbf{L}^T) - \mathbf{I} p) = \nabla \cdot (\boldsymbol{\tau} - \mu(\mathbf{L} + \mathbf{L}^T)), \quad (14)$$

where \mathbf{L} is the deformation rate tensor, and μ is a viscosity related to the low-rate shear viscosity of the polymer (see Ref.[27]). The standard Galerkin procedure is applied to equation (14), that is the terms are multiplied by the finite element interpolation functions, φ_i , followed by integration by parts over the problem volume. Details of the finite element formulation are given in Ref. [27]. The integration is performed using '3-point Gaussian integration' which means evaluating each term at 27 Gauss points per element in 3-D (as opposed to the 9 Gauss points needed for 2-D). The finite element formulation produces a stiffness matrix from the left hand side of equation (14), and a force vector from the right hand side. The force vector is computed at the end of each full-field stress computation, and the resulting system of equations is used to update the velocity and pressure fields. The stress is then re-computed at all points as described above, and an iterative procedure follows until satisfactory convergence is obtained. In this work we obtained relative convergence of at least 3×10^{-4} for velocity components at all rates, and 4×10^{-4} for relative pressure convergence.

Computation of the z-symmetry plane streamfunction

The streamfunction, ψ , defined by $\partial\psi/\partial y = u$ and $\partial\psi/\partial x = -v$ is valid in 2-D and axisymmetric flows, but is not generally valid in 3-D flows due to velocity gradients in the z-direction. For the current problem, however, the streamfunction is valid on the $z = 0$ plane; this is because the z-direction velocity gradient in the z-direction ($\partial w/\partial z$) is zero on this plane, and so the mass continuity equation ($\partial u/\partial x + \partial v/\partial y + \partial w/\partial z = 0$) reduces to $\partial u/\partial x + \partial v/\partial y = 0$. Because of this a streamfunction can be computed on the plane $z = 0$ by substituting the equations that define ψ into the reduced mass continuity equation, giving

$$\frac{\partial}{\partial x} \left(\frac{\partial \psi}{\partial y} \right) - \frac{\partial}{\partial y} \left(\frac{\partial \psi}{\partial x} \right) = 0, \quad (15)$$

subject to the boundary condition $\psi = 0$ on the upper outer surface of the die. Calculating streamfunction is of great use for visualising flows, and measuring opening angles, on the symmetry plane.

Computation of the birefringence pattern

In order to compare simulation stresses with experimental birefringence measurements, stress-birefringence equivalent plots were produced from the 3-D simulated results using the method of Clemeur et al [16]. In this method a Mueller matrix is integrated along a line of sight through the polymer. For calculation of birefringence in the x-y plane the Mueller matrix, $\mathbf{M}(z)$, starts equal to \mathbf{I} , where \mathbf{I} is the 4x4 identity matrix. The Mueller matrix is calculated by integration along a line in the z-direction, according to

$$\frac{d\mathbf{M}(z)}{dz} = \mathbf{m}(z) \cdot \mathbf{M}(z), \quad (16)$$

where $\mathbf{m}(z)$ is a matrix whose terms are built up from the stress components acting normally to z , and also uses the wavelength of the illuminating light and the stress optical coefficient C (see [16] for details). The method calculates the cosine of the birefringence retardation angle, δ , and the intensity can then be plotted proportional to $1 - \cos(\delta)$ [16]. This formula directly gives a dark fringe when

stress and thus δ are zero, and is consistent with orientating the polarisers at 90° to each other (i.e. “crossed” polarisers) whereas our birefringence equipment was adjusted to pass maximum light at zero stress (i.e. “uncrossed” polarisers). This suggests a π radians phase shift added to δ in order to plot light intensities that correspond to the experimental fringes. Additionally the polymer will have some ‘history’ from passing through an extruder screw on the way to the die that is essentially unknown, and which must contribute some phase shift in the birefringence. Hence, we accommodate a phase shift by plotting intensity proportional to $1 - \cos(\delta + \theta)$ where θ is the phase shift. Ref [30] gives a reliable method to extract the retardation angle from the Mueller matrix. In the work that follows the value of θ was found by adjusting θ until the first clear experimental fringe is aligned with the corresponding computed fringe.

5. 3-D simulation and comparison with experimental results

The experimental measurements were made at extruder screw rates of 5, 10, 15, 25 and 40 rpm. Measurement of the polymer output gave the corresponding mass flow rates as 14.4 g/min, 28.8 g/min, 43.0 g/min, 73.3 g/min and 117.3 g/min. The density of Lupolen 1840H at 150°C was measured to be 780 kg/m^3 [31]. From this the volumetric flow rate, Q , can be determined for each mass flow rate and the apparent shear rate, $\dot{\gamma}_a$, can be calculated according to

$$\dot{\gamma}_a = \frac{6Q}{W(2h)^2}, \quad (17)$$

where W is the width of the flow, and $2h$ is the slit height downstream of the die lip.

Table 2 lists the corresponding mass flow rates, volumetric flow rates and apparent shear rates.

Mass flow rate (g / min)	14.4	28.8	43.0	73.3	117.3
Q (m^3 / s)	3.08×10^{-7}	6.15×10^{-7}	9.19×10^{-7}	1.57×10^{-6}	2.51×10^{-6}
$\dot{\gamma}_a$ (/s)	5.25	10.5	15.7	26.7	42.8

Table 2 Relationship between mass and volumetric flow rates, and apparent shear rates.

Two planes of symmetry were used which reduces the problem to modelling one quarter of the volume of the die. Symmetry boundary conditions were applied ($w=0$ on the z symmetry plane defined by $z=0$, and $v=0$ on the y symmetry plane defined by $y=0$). Figure 7 shows the mesh, which contains 1010 elements, and 9713 nodes.

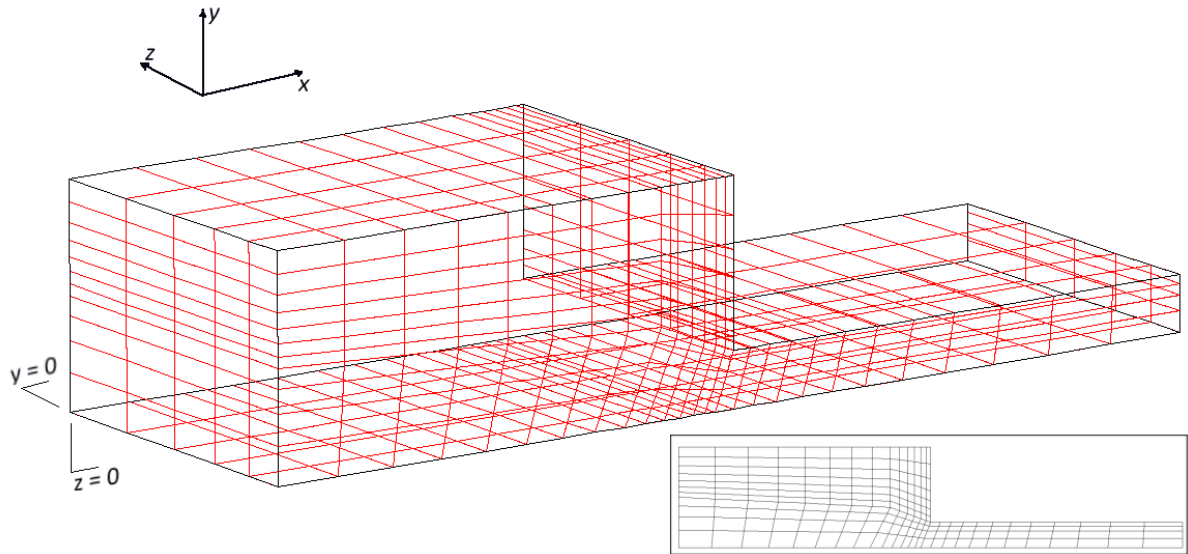


Figure 7 Mesh of 27-noded tri-quadratic elements, with planes of symmetry indicated. Inset: cross-section of mesh in x-y plane.

Non-slip boundary conditions ($u = v = w = 0$) were applied to the walls of the die. The inlet flow velocity was set using a two dimensional parabolic equation of the form

$$u = c \left(1 - \left(\frac{z}{(W/2)} \right)^2 \right) \left(1 - \left(\frac{y}{(H/2)} \right)^2 \right), \quad (18)$$

where H is the overall height at the inlet (ie.15 mm from Figure 1), and c is a value that can be varied to give any required volumetric flow rate.

Comparison of Opening Angles

Figure 8 shows the streak photographs at flow rates of 14.4, 43.0 and 117.3 g/min. At each flow rate the opening angles were measured above and below the centreline, and the two measurements averaged to give the final figure.

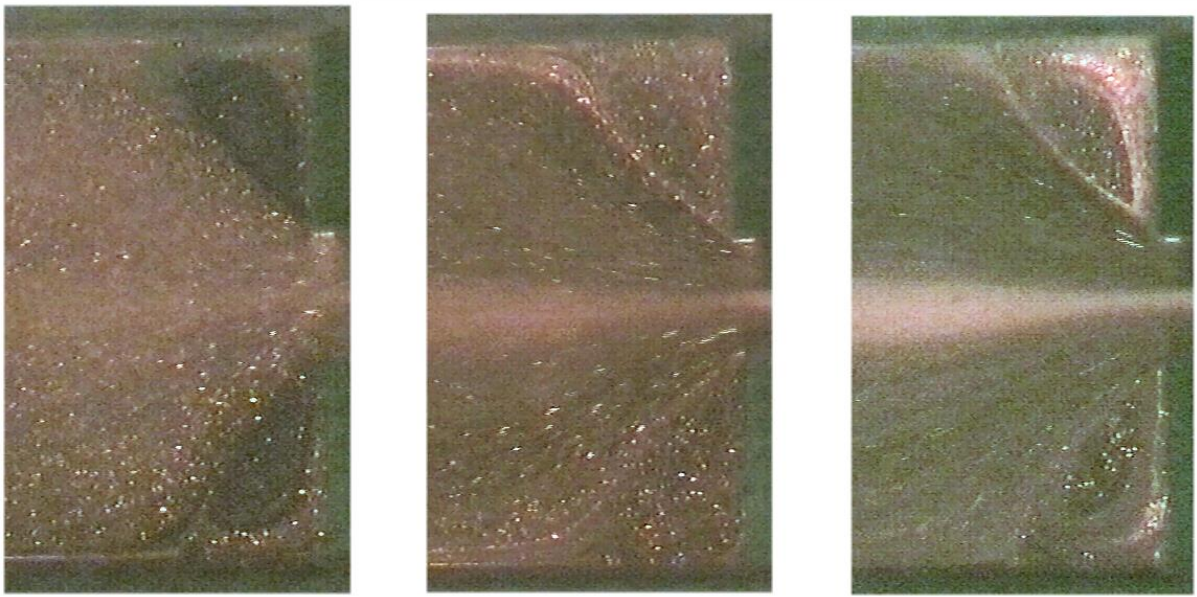


Figure 8 Streak photographs at mass flow rates of 14.4, 43.0 and 117.3 grams per minute from left to right, corresponding to apparent shear rates of 5.25, 15.7 and 42.8 s^{-1} .

Figure 9 shows measurement of the opening angles from simulation using a software cursor in conjunction with the velocity vectors, and the symmetry plane streamfunction (on $z = 0$). The velocity vectors are plotted with the *logarithm* of their speed giving the length of the velocity vector. This logarithmic scale allows the nodes with lower associated velocities, in particular those within the vortex, to be seen more clearly. The streamfunction on the $z=0$ plane was used as the primary method of measuring opening angle, with confirmation given by the velocity vectors.

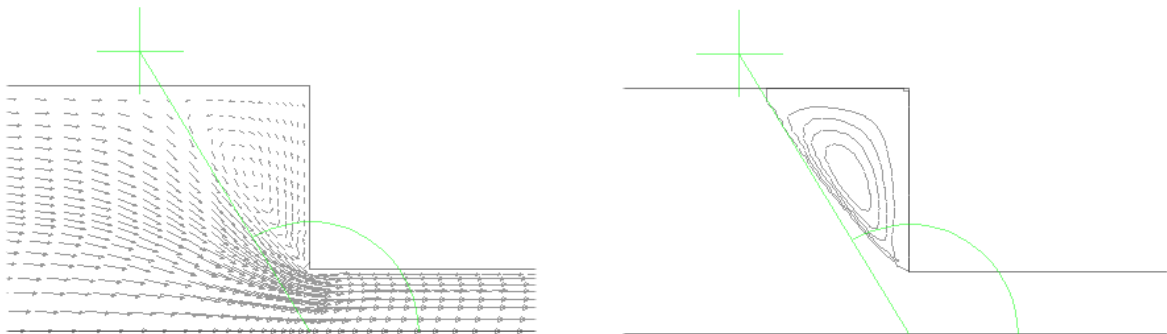


Figure 9 Indicating the measurement method using logarithmically scaled velocity vectors (left) and the streamfunction that is valid on the $z=0$ plane (right). The results shown are for a flow of 14.4 g/min using convective constraint release mechanism CR2.

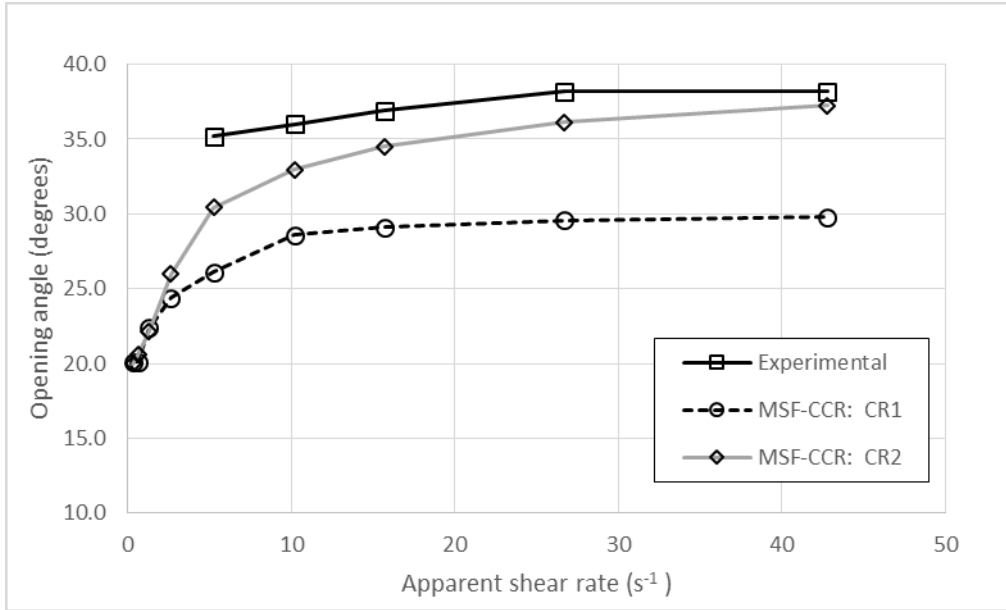


Figure 10 Comparison between experimental results and simulation results for the MSF-CCR model, using CR1 and CR2.

Figure 10 compares opening angles between experimental results and simulation using the MSF-CCR model with convective constraint release mechanisms CR1 and CR2. The opening angle over this range increases from approximately 35° to approximately 38°. The simulations using convective constraint release CR1 show a steady increase of opening angle with apparent shear rate but remain significantly below the experimental results, an approximately constant 8° lower over the range of the experimental data. The simulations using convective constraint release mechanism CR2 are above the CR1 results, except at very low apparent shear rates where both methods tend towards the Newtonian solution. The CR2 opening angles almost reach the level of the experimental results by the highest apparent shear rate (which corresponds to a flow of 117.3 g/min). Overall the CR2 convective constraint release mechanism is seen to capture the size and tendency of vortex opening angles more closely than CR1.

Comparison of birefringence results

Birefringence images were computed directly from the 3-D simulation results using the method of Clemeur et al. given in an earlier section. A difficulty in birefringence comparisons is obtaining a reliable value for the stress optical coefficient, C . A value of $C=1.12 \times 10^{-9} \text{ m}^2/\text{N}$ was determined for Lupolen 1840H LDPE from contraction flow birefringence measurements in Ref. [13]. Kiriakidis et al [12] reported variations of around 40% in stress optical coefficients obtained using different methods. Given the difficulties in obtaining a reliable value, the value of C is often taken to be *around* $2 \times 10^{-9} \text{ m}^2/\text{N}$ [32].

In planar flows one approach is to assume a value of the stress optical coefficient, C , such that

$$\Delta\sigma = \sigma_I - \sigma_{II} = \frac{k\lambda}{CW} \quad (19)$$

where $\sigma_I - \sigma_{II}$ is the computed principal stress difference at a point, k is the experimental fringe order at that same point, λ is the wavelength and W is the depth of the sample through which the

light ray passes [18]. In 3-D the situation is more complex since the light rays pass through a continuum of layers with different stress values, however a similar approach can be used by finding a value of the stress optical coefficient, C , that matches the 3-D computed fringes to the experimental fringes. In preliminary experiments it was found that a constant value of C could give only a qualitative fit at all rates, hence an independent *apparent* value of C was used at each rate. A similar finding is suggested in the work of Clemeur et al. [16] who found that the apparent value of C varied by over a factor of 2 for results whose apparent shear rates varied by a factor of 10 [16]. In this work we calculate C at each flow rate by matching the number of fringes measured and computed along the centreline. The apparent variation of C is reviewed later in this work.

A comparison of results obtained from experiment and results from simulation using convective constraint release CR1 are shown in Figure 11. Corresponding results for CR2 are shown in Figure 12. At each flow rate the initial phase angle θ (see equation 16 and the text following it) was found by matching the first distinct experimental fringe to the corresponding computed fringe (the initial process used an assumed value of the stress optical coefficient). Following this a value of the stress optical coefficient, C , was found such that the number of centreline fringes at that rate were matched. Hence two parameters were used in matching the computed and experimental birefringence patterns. The first parameter θ (the initial birefringence phase angle) effectively matches the position of the first clear fringe, and the second parameter C (the apparent stress optical coefficient) matches the *order* of the peak fringe on the centreline, but not necessarily its position. For CR1 the values of C so obtained varied from $2.08 \times 10^{-9} \text{ m}^2/\text{N}$, at the lowest flow rate to $1.58 \times 10^{-9} \text{ m}^2/\text{N}$ at the highest flow rate. This indicates a factor of 1.32 variation of the *apparent* stress optical coefficient from a factor of 8.0 change in apparent shear rate. For CR2 the corresponding values are from $1.63 \times 10^{-9} \text{ m}^2/\text{N}$ to $1.15 \times 10^{-9} \text{ m}^2/\text{N}$ showing a variation by a factor of 1.42. For both CR1 and CR2 the experimental (left) and simulated (right) birefringence images show overall similar patterns with the 'bow' shapes converging towards the slits, and a high peak in stress near the lip of the contraction. For CR1 at the two lower rates there are the same number of stress fringes at the lip for both experiment and simulation, with a tendency for an extra simulation fringe as the rates increase. For CR2 there is a clear tendency to over-predict the number of fringes near the lip. Stress relaxation can be seen on the centreline downstream of the contraction, at all rates and for both models there is very good correspondence between experiment and simulation in the number and separation of fringes during relaxation. Both models show a difference from experiment on the walls near the inlet, where there appear to be additional fringes from the simulation. This may be due to effects of the inlet boundary conditions being parabolic, and not a precise match to a fully developed profile for the polymer. The stress patterns downstream of the peaks near the lips also show an interesting difference. The experimental results show significant 'stress fangs' (as the stresses that appear to be convected downstream of the peaks near the lips are sometimes called) whereas the CR1 simulated fringe patterns lack this feature at all rates. The CR2 results on the other hand show this 'stress fangs' pattern clearly.

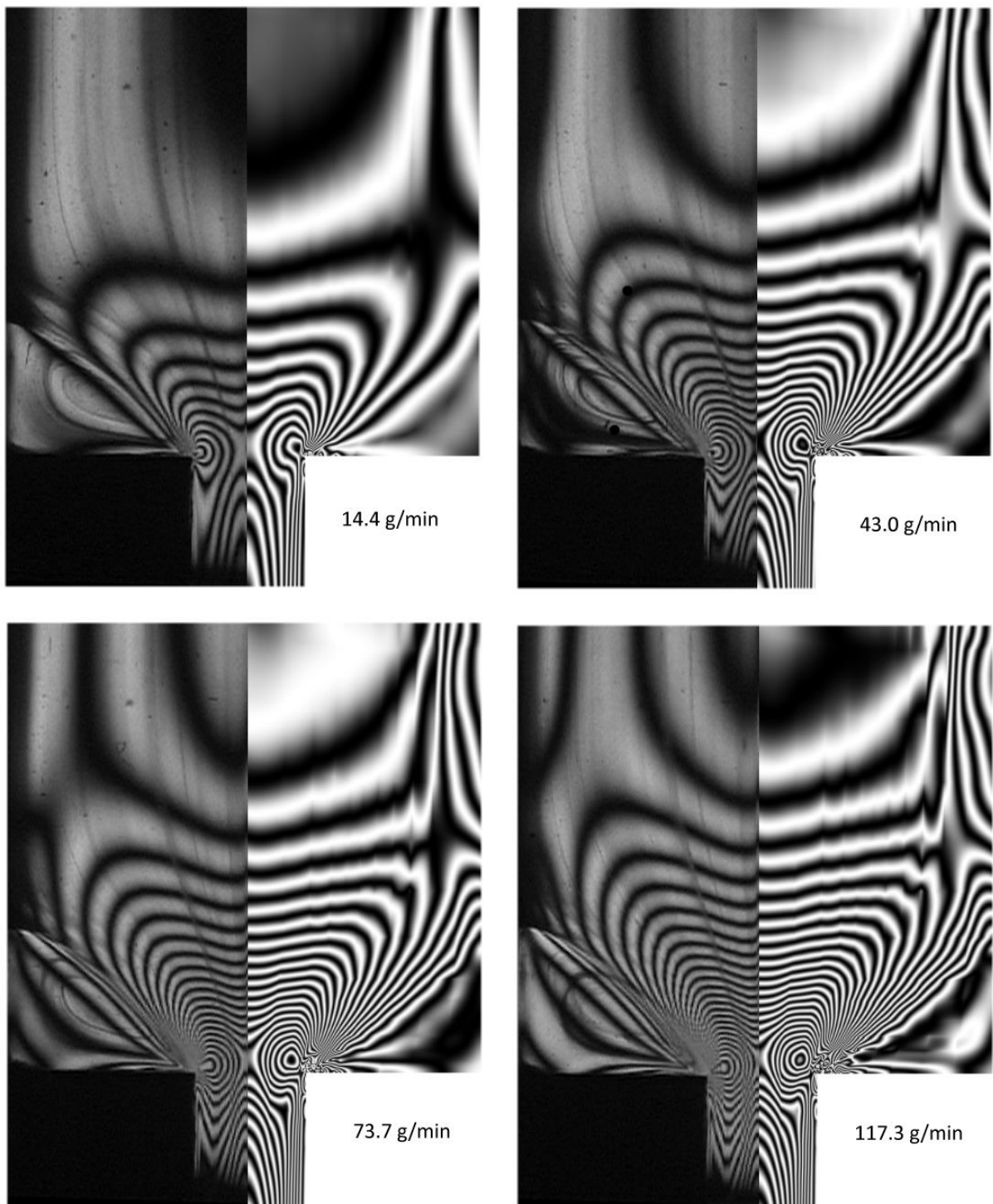


Figure 11 Comparison between experimental (left) and computed (right) birefringence images using convective constraint release CR1 for a range of flow rates (flow rates, in ascending order, correspond to apparent shear rates of $5.25s^{-1}$, $15.7s^{-1}$, $26.7s^{-1}$ and $42.8s^{-1}$).

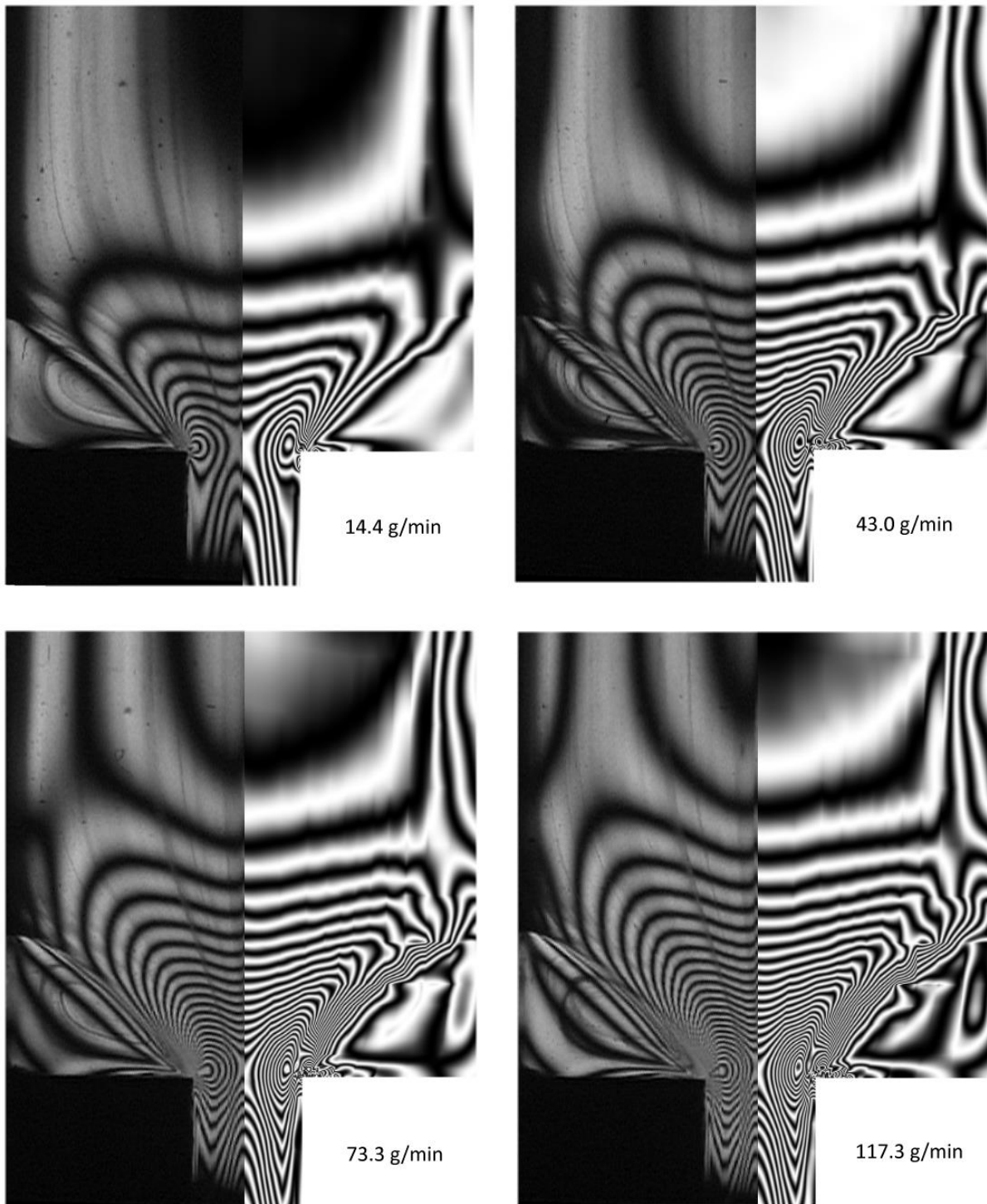


Figure 12 Comparison between experimental (left) and computed (right) birefringence images using convective constraint release CR2 for a range of flow rates (flow rates, in ascending order, correspond to apparent shear rates of $5.25s^{-1}$, $15.7s^{-1}$, $26.7s^{-1}$ and $42.8s^{-1}$).

Figure 13 compares the best-fit values of stress optical coefficient as obtained over all shear rates, for CCRs: CR1 and CR2. For the CCRs the best-fit values fall with apparent shear rate by a factor of approximately 1.3 - 1.4 over a factor of 8.0 in apparent shear rates. Comparison between experimental birefringence results (over a comparable factor of apparent shear rates (10.0)) and the DCPD and UCM models (see Ref. 16) produced values of the stress optical coefficient that changed by factors of approximately 2.2 and 70 respectively. The current comparison thus shows less variation in the

apparent value of stress optical coefficient. Two characteristics stand out however, the apparent stress optical coefficients for CR2 are consistently lower than those for CR1 (implying greater predicted stresses for CR2), and the coefficients consistently reduce with apparent shear rate. These features are now considered in turn.

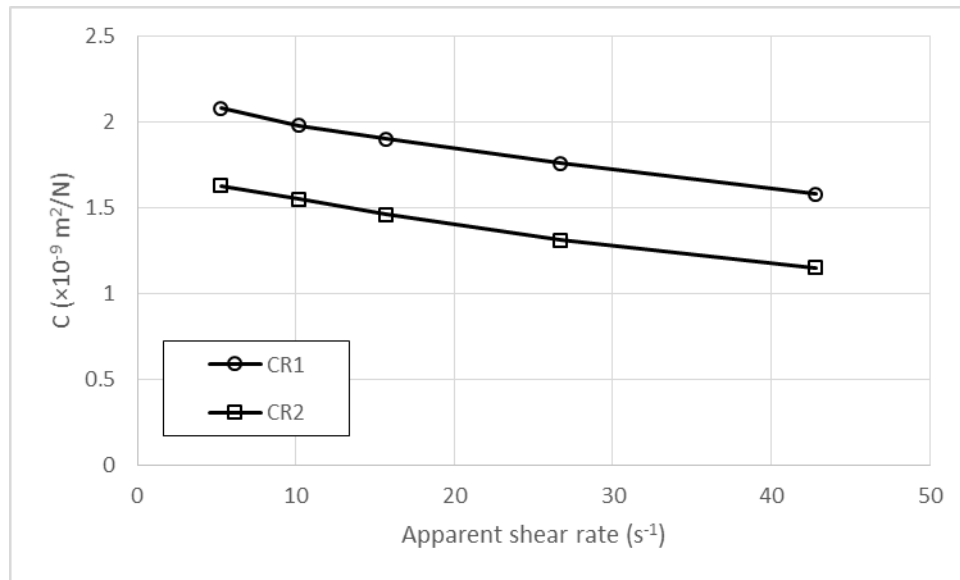


Figure 13 Comparison of apparent best-fit values of the stress optical coefficient, C , obtained at different apparent shear rates for CCRs CR1 and CR2.

The difference between CR1 and CR2 along the centreline is of particular interest as these two CCR mechanisms give identical results in *constant rate* elongation. The deformation along the centreline is purely elongational, but the rate of elongation changes along the path. Figure 14 compares the centreline elongational rates from simulation for both CR1 and CR2. It is seen that CR2 gives significantly higher elongational rates than CR1 near the contraction, with slightly lower elongational rates at earlier times. The elongational rates are of the order of 15% higher for CR2 at all rates, which could account for CR2 stresses being higher. An additional factor is that the centreline flow regimes are clearly not 'constant rate' and so the DA_1/Dt term in equation (8) will have an effect in elongation. A likely cause of the increased elongational rates approaching the lip is the greater opening angles simulated using CR2 which will tend to cause (or indicate) compression of the polymer later in its path towards the contraction. Another indicator is considered: careful comparison of Figures 11 and 12 seems to show that CR2 gives a consistently closer match between experimental and simulation fringes along the centreline (even after recalling that the first fringe's position and the peak fringe's order are matched in determining the value of stress optical coefficient). In particular the fringe matches are best at the higher flow rates for CR2, and these flow rates are the flow rates where the predicted opening angles are closest to the experimental opening angles. It looks very likely that the opening angle is significantly affecting centreline elongational rates and the resulting stresses, and thus affecting the apparent stress optical coefficients.

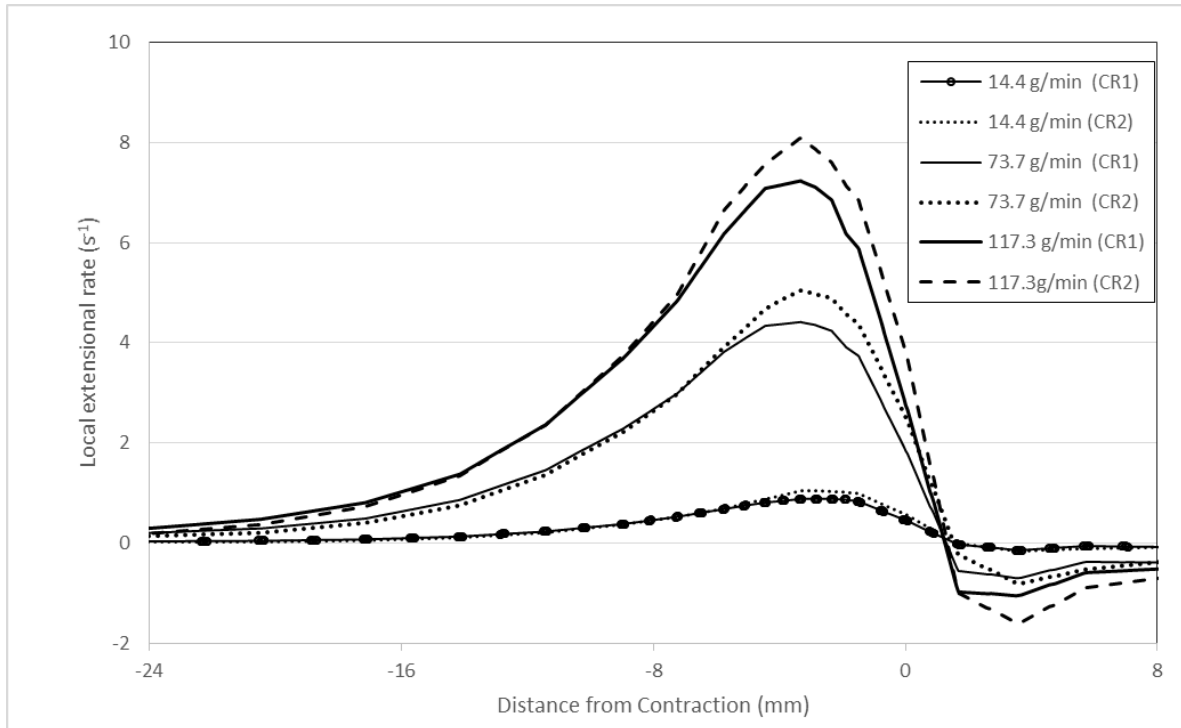


Figure 14 Elongational rates along the centreline from simulation, for a range of flow rates.

The cause of the apparent stress optical coefficient falling with apparent shear rate (for both CR1 and CR2) is now considered. The first consideration comes from the observation that the elongational predictions of the MSF-CCR showed some differences to rheometric data at higher rates in Figure 5.

As can be estimated from Figure 14, peak elongational rates in the simulations vary from approximately 1 s^{-1} at the lowest flow rate to 8 s^{-1} at the highest simulated rate. Also for a 4:1 contraction, the stretch ratio along the centreline should be approximately 4, or a Hencky strain of approximately 1.38 (because Hencky strain equals the natural logarithm of stretch ratio in elongation). The differences between the experimental rheometric results and MSF-CCR predictions were then estimated at the peak centreline elongation rates and a Hencky strain of 1.38. The differences were found to be sufficient to account for a factor of around 1.1 over the range of flow rates, but insufficient to account for the observed factor of 1.3 - 1.4 as is shown in Figure 13. The stress optical law is regarded as “semi-empirical” [16], so it is worth considering the possibility that the stress optical coefficient might vary with factors other than temperature. However the deviations reported in refs. [21] and [22] occur beyond a strain of 2, which is greater than the centreline strain in these flows. It is worth noting that the range of change in apparent stress optical coefficient obtained using the MSF-CCR is less than that noted in work comparing other constitutive models, where variation has been quantitatively assessed.

It is interesting to look at some 3-D aspects of the simulation. Figure 15 compares vortex details for planes ranging from the centreline to the side wall (at 73.3 g/min using CR2). As discussed earlier, streamfunction is only valid on the centre plane and so velocity vectors are shown. The lengths of the vectors are scaled to the logarithm of speed in order to show vortex details; the scale is the same for all four planes. The plots are shown at fractions of 0%, 30%, 60% and 90% of the distance to the side wall (the percentage value is nominal: the mesh plane nearest to the given percentage is shown). The plot shows there are only slight differences between the centre plane and the plane 60% of the

distance to the wall. Very close to the wall (90% nominal) the vortex area is still large, indeed slightly larger than at the symmetry plane, but with a changed shape and the vortex centre has moved very close to the lip.

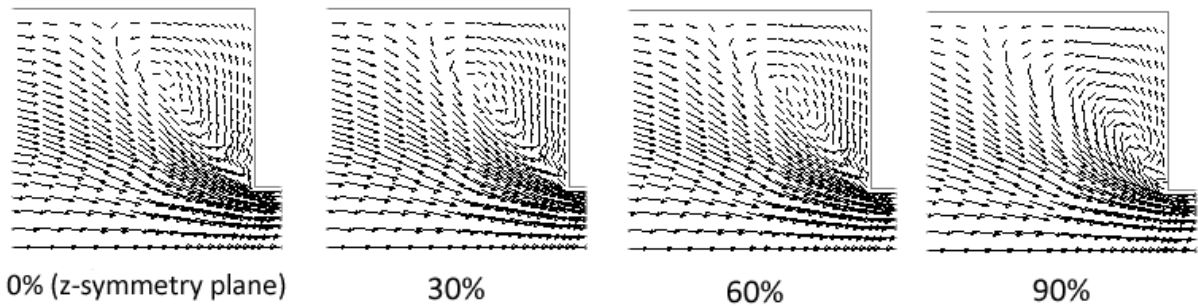


Figure 15 Comparison of velocity vectors at 73.3 g/min using CR2 (vector length logarithmically scaled to speed) at different distances from the z-symmetry plane. 0% corresponds to the symmetry plane, 100% would correspond to the side wall.

Birefringence calculation involves computing an integral along a line-of-sight through the polymer (as outlined earlier), and so would be expected to be significantly changed from 2-D results by the differences for a 5:3 ratio die. Figure 16 compares the birefringence patterns obtained from full 3-D computation with the equivalent from a 2-D flow with the same apparent shear rate. The apparent shear rate of the 2-D simulation is 26.7 s^{-1} corresponding to a flow of 73.7 g/min.



Figure 16 Comparison between 5:3 aspect ratio 3-D predictions (left) and 2-D predictions (right) at 73.7 g/min using convective constraint release mechanism CR2

A value of stress optical coefficient of $1.31 \times 10^{-9} \text{ m}^2/\text{N}$ was used to produce the 2-D birefringence pattern, as this was the value obtained for the 3-D case. Along the centreline the fringes for the 2-D and 3-D simulations tend to meet each other quite accurately (showing very similar stress levels along the centreline), but the 2-D fringes reach the centreline at a much 'steeper' angle. This may be viewed as an effect of the nearby side walls (in the 3-D case) reducing the sharpness of peaks in comparison to the 2-D solution. The vortex areas show perhaps most difference from each other, which is likely to be caused partly by the cross-sectional differences in vortex behaviour in 3-D, but also by the effects of the side walls on otherwise low stresses. The opening angle in 2-D is slightly greater (36.2° for the 3-D simulation and 39.7° for 2-D). A reasonable interpretation is that the effect of the side walls in the 3-D problem is to suppress vortex behaviour by a frictional effect.

To investigate the differences between 2-D and 3-D further, equivalent birefringence patterns from slices across the flow were generated. This is not practicable experimentally because birefringence patterns result from an optical path through the full flow, but as will be shown can be investigated numerically. The slices used were each 1% of the total width of the die and were chosen at planes corresponding to those used in Figure 15. To compensate for the large fractional reduction in slice thickness the wavelength was reduced in calculations by the same proportion, in order to give directly comparable retardation angles. The results are shown in Figure 17.

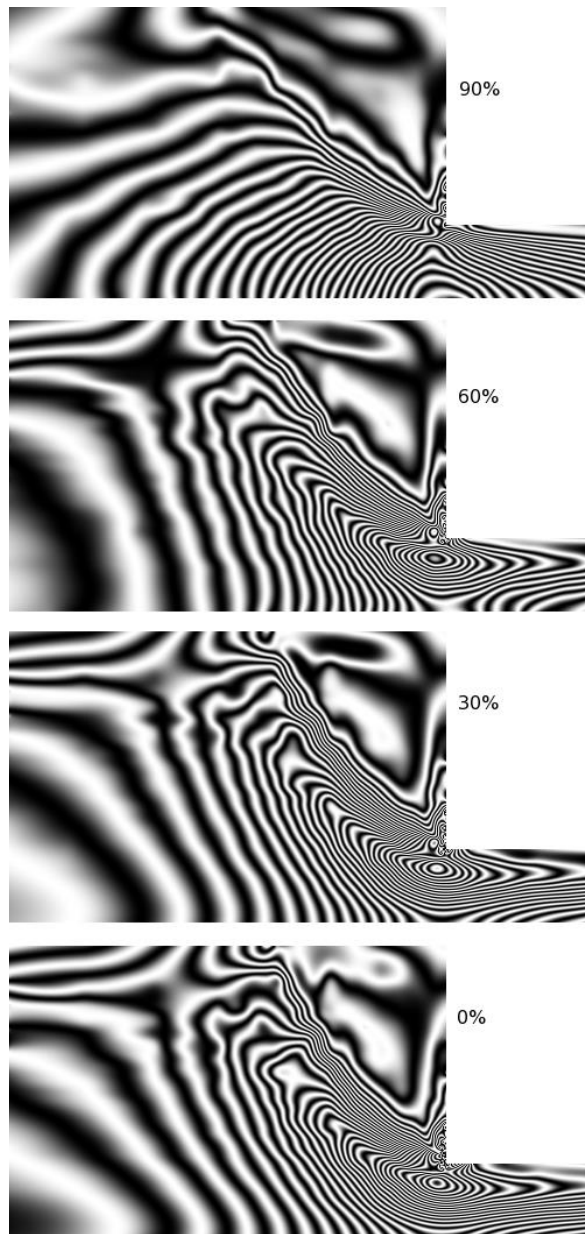


Figure 17 Comparison of birefringence at 73.3 g/min, using CR2, at different distances from the z-symmetry plane. 0% corresponds to the z-symmetry plane, 100% would correspond to the side wall.

Figure 17 shows a marked change of behaviour between the symmetry plane and the side wall. The birefringence from the symmetry plane (marked “0%” in Figure 17) meet the centreline at a ‘steep’ angle, rather similarly to the 2-D simulation. This is accounted for by the symmetry plane being the plane that is most independent from the 3-D effects of the wall. The birefringence from near the wall shows a profoundly different pattern; the stresses underlying these patterns effectively ‘add’ to give the patterns seen in the 3-D result in Figure 16. It is again evident that the differences between the 0% plane and the 60% plane are fairly minor.

6. Discussion and Conclusions

The Molecular Stress Function model with Convective Constraint release (MSF-CCR) is derived from energy balance considerations and, with only two adjustable parameters, gives an excellent fit to rheological measurements in shear and also in uniaxial, biaxial and planar elongation, and has been shown to give strong vortex growth in planar and asymmetrical abrupt contraction flows (see Ref. [6]).

This work shows the model also gives comparable vortex growth and birefringence to experiment in an abrupt contraction flow with significant 3-D effects caused by a small aspect ratio.

The 3-D implementation of the MSF-CCR is a 3-D extrapolation of the method described in Ref. [6] which was for 2-D and asymmetrical flows. The 3-D implementation addresses a number of differences that arise from specific aspects of a 3-D flow. The largest difference arises from the lack a general streamfunction in 3-D which prevents use of the (streamfunction based) streamline correction tracking of the 2-D / axisymmetric implementation. A purely kinematic tracking method was used instead, which brings a potential for inaccuracies in tracking due to the (implied) *finite* accuracy that is possible with a finite element method (FEM). Although finite accuracy is naturally accepted when using the FEM, a finite accuracy of tracking has the potential to cause significant errors if a particle is tracked back into a collision with a wall. The effects of this could be assessed directly in 2-D by comparing two sets of simulations for the same flows; one using streamline tracking and one with kinematic tracking only. The differences were found to be small over a large range of flow rates, with a maximum difference of 0.5° in opening angle at any flow rate, and differences in contours of principal stress difference were found to be very slight. This latter point is important when birefringence is to be compared with experiment as contours of principal stress difference in 2-D are proportional to contours of constant birefringence retardation angle (per unit depth), and thus can be viewed as equivalent to birefringence fringes themselves.

In this work a 4:1 ratio abrupt contraction flow was studied experimentally. This flow can be expected to have strong 3-D characteristics due to the 5:3 aspect ratio. The 3-D implementation of the MSF-CCR was compared with the results using two versions of the convective constraint release. Experimentally the flow gives a strong vortex and vortex growth with increasing flow rate. It is shown that the MSF-CCR model in 3-D also gives strong growth in this geometry. This vortex growth is most closely captured by simulations using the convective constraint release mechanism named CR2. The simulation opening angles rise less quickly than experiment (similar to behaviour of IUPAC Melt A LDPE in axisymmetric flow as shown in Ref.[6]) but reach a similar level at an apparent shear rate of approximately 40 s^{-1} . Simulation was able to show further that the flow has an approximately constant cross section across approximately 60% of its width.

Birefringence results brought out other characteristics. Both of the convective constraint release mechanisms studied, CR1 and CR2, gave a good overall match, but each had its stronger and weaker points. The mechanism CR1 gave the closer match to the peak stress in the main flow near the lip of the contraction but showed little sign of 'stress fangs' downstream of this peak. CR2 on the other hand reliably predicted stress fangs but over-predicted the size of the peak stress near the lip.

Stress optical coefficients were chosen at each flow rate by matching the first clear experimental fringe to simulation using an offset angle and then matching the order of the peak fringe (but not its position). The values of stress optical coefficient that gave best comparison between experiment and simulation were found to vary by up to 40% over a range of apparent shear rates that were varied by a factor of 8.0. The apparent stress optical coefficients (obtained from a peak centreline stress match) for CR2 were consistently lower than those obtained for CR1, due to higher centreline stresses using CR2. These higher centreline stresses were found to be caused chiefly by higher centreline elongational rates, and evidence was found these higher elongational rates were in turn caused by (or at least related to) higher opening angles. It was noted that the simulations whose opening angles were closest to the experimental opening angles also gave the best detail match to birefringence fringes along the centreline. A key point is that opening angle has a strong effect on the value of apparent stress optical coefficient that is measured and needs to be matched if possible. From the

current simulations the best match to both opening angle and birefringence patterns is found at 117.3 g/min using convective constraint release mechanism CR2, and that gives a value of $1.15 \times 10^{-9} \text{ m}^2/\text{N}$ for Lupolen 1840H LDPE. This is remarkably close to the value of $1.12 \times 10^{-9} \text{ m}^2/\text{N}$ given in Ref. [13] using an 8:1 abrupt contraction slit.

A comparison between 3-D simulation and 2-D simulation at a fixed apparent shear rate showed similar vortex opening angles in both cases. The 3-D opening angle was slightly lower than the 2-D which may be explained by the 'drag' of the side walls suppressing vortex behaviour in a 5:3 aspect ratio die. The fringes along the centreline met quite accurately (using the same value of apparent stress optical coefficient), but with a significant difference in the angle at which the fringes approached the centreline. An examination of the birefringence from different slices through the plane revealed effects from the edge to be a major cause of the difference.

A number of comparable assessments in contraction flows have been conducted for other constitutive models that fit a wide range of rheometric data well, such as the Pom-pom model. The eXtended Pom-pom (XPP) model was shown to give qualitative agreement for vortex growth in an abrupt contraction flow of IUPAC A polymer melt [33]; however birefringence was not compared. The Double Convected Pom-pom (DCPP) model was used to simulate flow of a commercial LDPE through a planar contraction [34]. Good agreement was shown for velocity and principal stress difference (PSD) along the centreline of the flow, and a parametric study showed how vortex area varied with model parameters. No comparison with experimental vortex area was made in the study. Tenchev et al. [35] compared many models, including the XPP for a 4:1 abrupt contraction flow of commercial polystyrene. Cross-sectional velocity components were in good agreement with experiment, with a qualitative agreement shown for birefringence. Boukellal et al. [18] used another tube-based model, that of Marrucci and Ianniruberto [36], which also uses a Convective Constraint Release (CCR) mechanism, to simulate a semi-circular converging flow of polystyrene. Birefringence measurements, and velocity measurements using Laser Doppler Velocimetry, were compared and shown to agree well with experiment.

The current assessment is a demanding one as it compares the MSF-CCR model with measurements for two quantities which are both very sensitive to polymer properties, namely vortex opening angles and birefringence patterns. The MSF-CCR has the ability to fit rheometric data for a commercial LDPE with only two adjustable parameters, and from these has been shown to simulate vortex growth and birefringence for a 3-D abrupt contraction flow, that are comparable to experiment. The experimental data for vortex opening angles and birefringence that are given in this work, along with the rheological data for the material, would constitute a good test for any polymer constitutive model.

Appendix 1 Comparison of results with and without streamfunction tracking

In 3-D problems there is no equivalent to the streamfunction in 2-D and axisymmetric problems. In 2-D and axisymmetric problems the stream function can be used to help avoid collisions with walls since, with appropriate boundary conditions, a contour of constant streamfunction should never impinge upon a wall.

As discussed in Section 4, when tracking a particle as described by equation (12) finite accuracy in tracking means that particles can deviate from their original streamline. In some cases particles which pass very close to a wall can actually collide with (or pass through) the wall. There may not then be a better option than to reposition the particle to where it passed through the wall, and then continue the time integration accordingly. Whether it is a minor tracking error that occurs, or a collision with a

wall, some degree of accuracy is lost. For 2-D and asymmetrical flows a streamfunction based 'correction' to the kinematic tracking process, such as that given in Ref. [37], can avoid the problem.

In a 3-D flow, however, a comparable streamfunction is not available. In the 3-D implementation described in this work kinematic tracking is used without the benefit of any streamfunction correction. We assess the importance of this by performing similar 2-D simulations, both with and without streamfunction tracking. The 3-D simulations in this work compute vortex opening angles and birefringence. We address accuracy for both in turn.

The material modelled was the well-characterised IUPAC Melt A LDPE (to which Lupolen 1840H is considered an 'analogue'), whose relaxation spectrum and parameters for convective constraint release mechanism CR2 are given in Ref. [6]. Vortex opening angle is assessed first. Figure A.1 compares the opening angles obtained at a range of apparent shear rates, both with and without streamfunction tracking, in a 2-D 4:1 abrupt contraction flow.

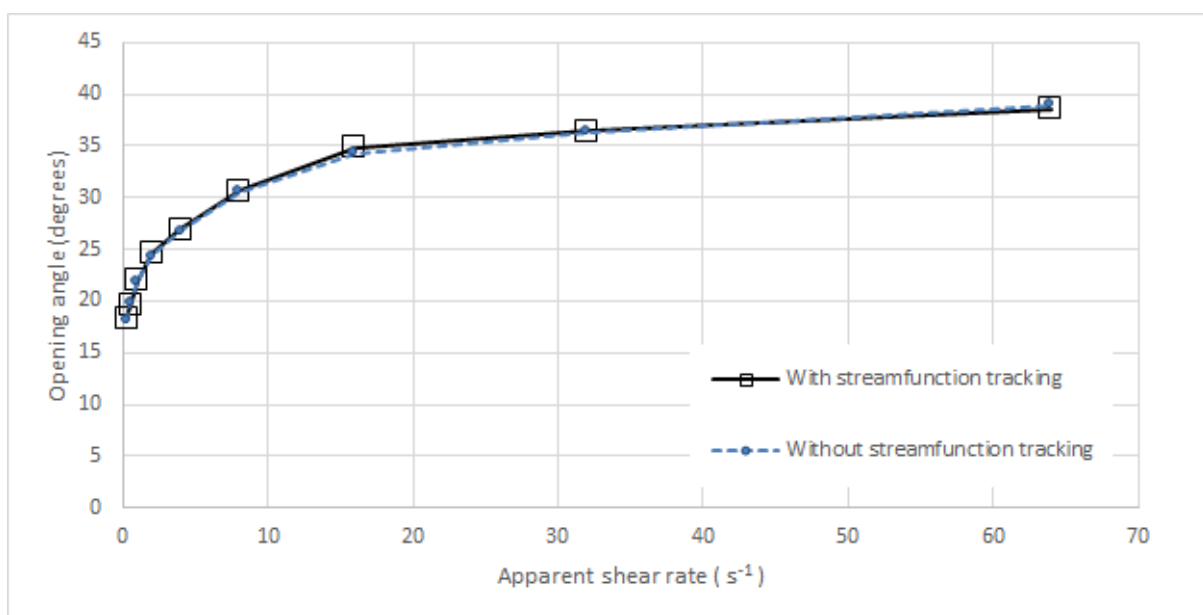


Figure A.1 Comparison of opening angles obtained in 2-D simulation with and without streamline tracking in a 4:1 abrupt contraction.

The results are very similar for the two tracking methods with a maximum difference of 0.52° at any rate, and an average difference of 0.25° . This suggests a maximum error of around 0.5° in determining vortex opening angles using kinematic tracking without a streamfunction tracking correction.

Birefringence patterns are closely linked to principal stress difference (PSD), and in truly planar flows the fringes correspond to contours of constant PSD. Because of this the variation in PSD was compared with and without streamfunction tracking. The PSD using the two methods at an apparent shear rate of $32 s^{-1}$ are shown side-by-side in Figure A.2

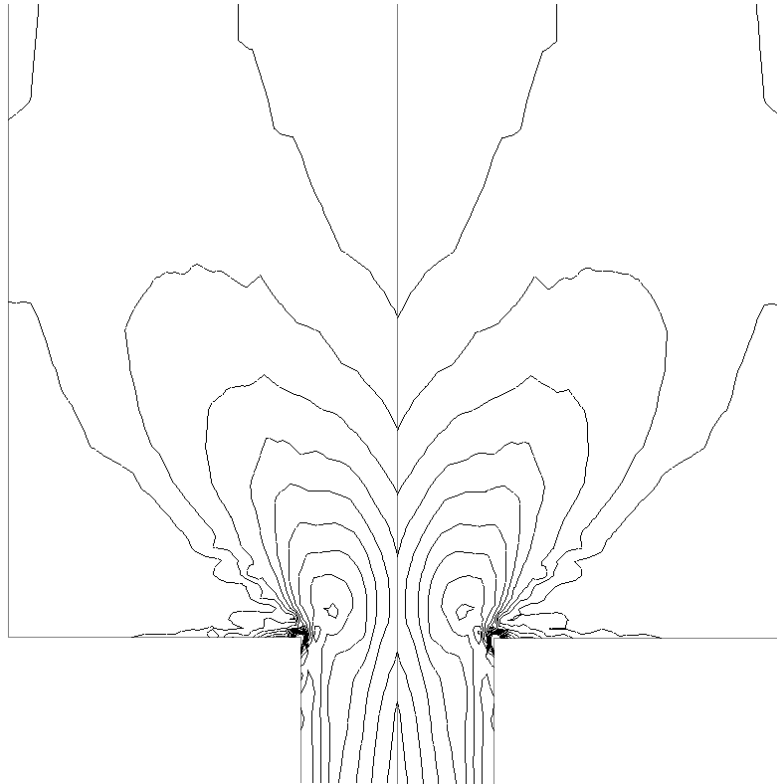


Figure A.2 Comparison of Principal Stress Difference for 2-D 4:1 contraction flow at an apparent shear rate of 32 s^{-1} with streamline tracking (left) and without streamline tracking (right). Contours are at multiples of 25kPa.

Difference in the PSD patterns are difficult to discern within the main flow, with more noticeable differences occurring in the vortex. The greater differences in the vortex area are not surprising because the particle paths undergo very tight turns in this region, making greater demands on kinematic tracking.

Overall, from Figure A.2 the computed PSD is only very slightly affected by the lack of streamfunction tracking, and there seems no reason to expect computed birefringence patterns to be more affected in 3-D flows.

References

- [1] M.H. Wagner, J. Schaeffer, Assessment of nonlinear strain measures for extensional and shearing flows of polymer melts, *J. Rheol. Acta* 33 (1994), 506.
- [2] M.H. Wagner, P. Ehrecke, P. Hachmann, J. Meissner, A constitutive analysis of uniaxial, equibiaxial and planar extension of a commercial linear high-density polyethylene melt, *J. Rheol.* 42 (1998), 621.
- [3] M.H. Wagner, H. Bastian, P. Hachmann, J. Meissner, S. Kurzbeck, H. Munstedt, F. Langouche, The strain-hardening behaviour of linear and long-chain branched polyolefin melts in extensional flows, *Rheol. Acta* 39 (2000), 97.
- [4] M.H. Wagner, P. Rubio, H. Bastian, The molecular stress function model for polydisperse polymer melts with dissipative convective constraint release, *J. Rheol.* 45 (2001), 1387.

- [5] G. Marrucci, Dynamics of entanglements: a nonlinear model consistent with the Cox–Merz rule, *J. Non-Newtonian Fluid Mech.* 62 (1996), 279.
- [6] P. Olley, M.H. Wagner, A modification of the convective constraint release mechanism in the molecular stress function model giving enhanced vortex growth, *J. Non-Newtonian Fluid Mech.*, 135, (2006), 68
- [7] T.C.B. McLeish, R.G. Larson, Molecular constitutive equations for a class of branched polymers: the Pom–Pom polymer, *J. Rheol.* 42 (1998) 81.
- [8] B. Robertson, R.L. Thompson, T.C.B. McLeish, I. Robinson, Polymer extrudate-swell: From monodisperse melts to polydispersity and flow-induced reduction in monomer friction. *J. Rheol.* 63(2) (2019), 319
- [9] W.M.H. Verbeeten, G.W.M. Peters, F.P.T. Baaijens, Numerical simulations of the planar contraction flow for a polyethylene melt using the XPP model, *J. Non-Newtonian Fluid Mech.* 117 (2004), 73.
- [10] M.G.H.M. Baltussen, W.M.H. Verbeeten, A.C.B. Bogaerds, M.A. Hulsen, G.W.M. Peters, Anisotropy parameter restrictions for the eXtended Pom-Pom model, *J. Non-Newtonian Fluid Mechanics*, 165, (2010), 1047.
- [11] R. Ahmed, R.F. Liang, M.R. Mackley, The experimental-observation and numerical prediction of planar entry flow and die swell for molten polyethylenes, *J. Non-Newtonian Fluid Mech.* 59 (1995), 129.
- [12] D.G Kiriakidis, H.J. Park, E. Mitsoulis, B. Vergnes, J.-F. Agassant, A study of stress distribution in contraction flows of an LLDPE melt, *J. Non-Newtonian Fluid Mech.*, 47 (1993), 339.
- [13] T. Gough, R. Spares, P.D. Coates, In-process measurements of full field stress birefringence and velocities in polymer melt flows, *Plastics Rubber and Composites*, (2005) 34:9, 393.
- [14] M.R. Mackley, M.W. Collins, The melt processing of monodisperse and polydisperse polystyrene melts within a slit entry and exit flow, *J. Non-Newtonian Fluid Mech.*, 128 (2005), 29.
- [15] T. Gough, R. Spares, A. L. Kelly, S.M. Brook, P.D. Coates, Three-dimensional characterisation of full field stress and velocity fields for polyethylene melt through abrupt contraction, *Plastics, Rubber and Composites*, 37, (2008), 158.
- [16] N. Clemeur, R.P.G. Rutgers, B. Debbaut, Numerical evaluation of three dimensional effects in planar flow birefringence, *J. Non-Newtonian Fluid Mech.*, 123 (2004), 105.
- [17] J.F.M. Schoonen, F.H.M. Swartjes, G.W.M. Peters, F.P.T. Baaijens, H.E.H. Meijer, A 3D numerical/experimental study on a stagnation flow of a polyisobutylene solution, *J. Non-Newtonian Fluid Mech*, 79 (1998), 529.
- [18] G. Boukellal, A. Durin, R. Valette, J.-F. Agassant, Evaluation of a tube-based constitutive equation using conventional and planar elongation flow optical rheometers, *Rheol. Acta*, 50 (2011), 547.
- [19] G. Boukellal, D. Hertel, R. Valette, H. Munstedt, J.-F. Agassant, Investigation of LDPE converging flows using fieldwise measurements techniques, *Symposium MS11: processing of polymers, Int. J. Mater. Form.* 1 (2008), 687.
- [20] R.G. Larson, *Constitutive Equations for Polymer Melts and Solutions*, Butterworths, Boston, 1988.

- [21] T. Sridhar, D.A. Nguyen, G.G. Fuller, Birefringence and stress growth in uniaxial extension of polymer solutions, *J. Non-Newtonian Fluid Mech.*, 90 (2000), 299.
- [22] C. Luap, M. Karlina, T. Schweizer, D.C. Venerus, Limit of validity of the stress-optical rule for polystyrene melts: Influence of polydispersity, *J. Non-Newtonian Fluid Mech.*, 138 (2006), 197.
- [23] A. Haghtalab, G. Sodeifian, Determination of the discrete relaxation spectrum for polybutadiene and polystyrene by a non-linear regression method, *Iran. Polym. J.* 11/2 (2002) 107.
- [24] M. Sentmanat, B.N. Wang, G.H. McKinley, Measuring the transient extensional rheology of polyethylene melts using the SER universal testing platform, *J. Rheol.* 49 (2005), 585.
- [25] H. Münstedt, S. Kurzbeck, L. Egersdörfer, Influence of molecular structure on rheological properties of polyethylenes—Part II: Elongational behavior, *Rheol. Acta* 37 (1998), 21.
- [26] M. Zatloukal, Differential viscoelastic constitutive equations for polymer melts in steady shear and elongational flows, *J. Non-Newtonian Fluid Mech.*, 113 (2003), 209.
- [27] P. Olley, A study of the quadratic molecular stress function constitutive model in simulation”, *J. Non-Newtonian Fluid Mech.*, 125 (2005), 171.
- [28] P.K. Currie, Constitutive equations for polymer melts predicted by the Doi–Edwards and Curtiss–Bird kinetic theory models, *J. Non-Newtonian Fluid Mech.* 11 (1982), 53.
- [29] M. Viriyayuthakorn, B. Caswell, Finite element simulation of viscoelastic flow, *J. Non-Newtonian Fluid Mech.*, 6 (1980), 245.
- [30] N. Ghosh, M.F.G. Wood, A. Vitkin, Mueller matrix decomposition for extraction of individual polarization parameters from complex turbid media exhibiting multiple scattering, optical activity, and linear birefringence, *J. of Biomedical Optics*, 13(4), (2008), 044036.
- [31] J. Meissner, J. Hostettler, A new elongational rheometer for polymer melts and other highly viscoelastic liquids, *Rheol. Acta* 33 (1994), 1.
- [32] O. O. Mykhaylyk, N.J. Warren, A.J. Parnell, G. Pfeifer, J. Laeuger, Applications of shear-induced polarized light imaging (SIPLI) technique for mechano-optical rheology of polymers and soft matter materials, *J. Polymer Science Part B: Polymer Physics* 54 (2016), 2151.
- [33] I. Sirakov, A. Ainsler, M. Haouche, J. Guillet, Three-dimensional numerical simulation of viscoelastic contraction flows using the Pom–Pom differential constitutive model, *J. Non-Newtonian Fluid Mech.*, 126, (2005), 163.
- [34] N. Clemeur, R. P. G. Rutgers, B. Debbau, Numerical simulation of abrupt contraction flows using the Double Convected Pom–Pom model, *J. Non-Newtonian Fluid Mech.*, 117, (2004), 193.
- [35] R. Tenchev, T. Gough, O. G. Harlen, P. K. Jimack, M. A. Walkley, Three dimensional finite element analysis of the flow of polymer melts, *J. Non-Newtonian Fluid Mech.*, 166, (2011), 307.
- [36] G. Marrucci, G. Ianniruberto, Flow-induced orientation and stretching of entangled polymers. *Philos. Trans. R. Soc. Lond. Ser A Math. Phys. Sci. Eng.*, 361, (2003), 677.

[37] P. Olley, An adaptation of the separable KBKZ equation for comparable response in planar and axisymmetric flow, *J. Non-Newtonian Fluid Mech.*, 95 (2000), 35.